ADVANCED OPTICAL MATERIALS
www.advopticalmat.de

# Tunable Resonant-Photopyroelectric Detector Using Chalcogenide–Metal–Fluoropolymer Nanograting

*Le Wei, Hosein Monshat, Jingjing Qian, Liang Dong,* and Meng Lu**

**Pyroelectric detectors are often broadband and require external filters for wavelength-specific applications. This paper reports a tunable, narrowband, and lightweight pyroelectric infrared detector built upon a flexible membrane of $As_2S_3$–Ag–P(VDF-TrFE) with subwavelength grating, which is capable of both on-chip filtering and photopyroelectric energy conversion. The top surface of this hybrid membrane is a corrugated $As_2S_3$–Ag film contributing to narrowband light absorption in the near-infrared (NIR) regime, and the bottom part is a polyvinylidene fluoride-trifluoroethylene (PVDF-TrFE) membrane for the conversion of the absorbed light to an electrical signal. Uniquely, applying a bias voltage to the PVDF-TrFE membrane enables the tuning of the device's absorption and pyroelectric characteristics owing to the piezoelectrically induced mechanical bending. The resonator exhibited a resonant absorption coefficient of 80% and a full-width-half-maximum of 15 nm within the NIR, a responsivity of 1.4 mV $mW^{-1}$, and an equivalent noise power of 13 μW $Hz^{-1/2}$ at 1560 nm. By applying a 15-V bias to the PVDF-TrFE membrane, the absorption coefficient decreased to 18% due to the change in the grating period and incident angle. The narrowband and tunable features of the $As_2S_3$–Ag–P(VDF-TrFE) pyroelectric detector will benefit a variety of potential applications in sensors, optical spectroscopy, and imaging.**

## 1. Introduction

Photopyroelectric detectors can absorb electromagnetic radiation, convert the absorbed energy into thermal energy, and generate a pyroelectric voltage (PEV) across a pyroelectric material.[1] They have been widely used in various applications, such as energy harvesting, infrared sensing, and thermal imaging.[2–7] When a photopyroelectric detector is optically heated or cooled, the pyroelectric material changes its polarization resulting in a transient PEV output. The amplitude of PEV depends on the ability of the detector to absorb light absorption, the degree of temperature change, and the pyroelectric coefficient. While many photopyroelectric detectors have been demonstrated to measure electromagnetic radiations over a broad spectral range from visible to terahertz,[8] narrowband photopyroelectric devices are highly desired as they are able to respond to infrared radiation in a specific wavelength range.[9–12]

Conventional narrowband photopyroelectric detectors require inserting a bulky, heavyweight bandpass filter in front of a broadband pyroelectric detector. Alternatively, a narrowband filter, such as the surface plasmon resonator, Bragg spectral filter, photonic crystal, or Whispering-gallery mode resonators, can be directly integrated with the pyroelectric sensing element.[13–15] Among these optical resonators, the planar photonic crystals, which can support the guided-mode resonance, are particularly interesting owing to the potential of integrating with most pyroelectric materials and coupling incident lights into a resonance mode via the grating modulation.[6,16–19] The photonic crystal-based gratings can not only display narrowband reflection or transmission but also support absorption resonance when a lossy material, such as thin metal film, is used as one of the cladding layers.[20,21] For applications in near- and mid-infrared, chalcogenide glasses can be adopted to build the photonic crystal grating and achieve resonance modes with a narrow bandwidth and high-quality factor.[22–24] However, toward a narrowband infrared photopyroelectric sensor, it is still challenging to integrate a chalcogenide-based photonic crystal with common pyroelectric materials, such as ferroelectric polymers. Most narrowband photopyroelectric detectors, once they were fabricated, have a fixed spectral position and bandwidth, which limit their ability to adapt to multi-spectral applications.

This paper reports a resonant-photopyroelectric detector (R-PED) that combines narrowband optical absorption and pyroelectric sensing functions on a free-standing membrane. The narrowband optical absorber consists of a 1D chalcogenide ($As_2S_3$) grating with a silver cladding layer. The photonic crystal absorber was fabricated on a polyvinylidene

L. Wei, J. Qian, L. Dong
Department of Electrical and Computer Engineering
Iowa State University
2115 Coover Hall, Ames, IA 50011, USA
E-mail: ldong@iastate.edu
H. Monshat, M. Lu
Department of Electrical and Computer Engineering
Department of Mechanical Engineering
Iowa State University
2128 Coover Hall, Ames, IA 50011, USA
E-mail: menglu@iastate.edu
The ORCID identification number(s) for the author(s) of this article can be found under https://doi.org/10.1002/adom.202101147.

© 2021 The Authors. Advanced Optical Materials published by Wiley-VCH GmbH. This is an open access article under the terms of the Creative Commons Attribution License, which permits use, distribution and reproduction in any medium, provided the original work is properly cited.

**DOI: 10.1002/adom.202101147**

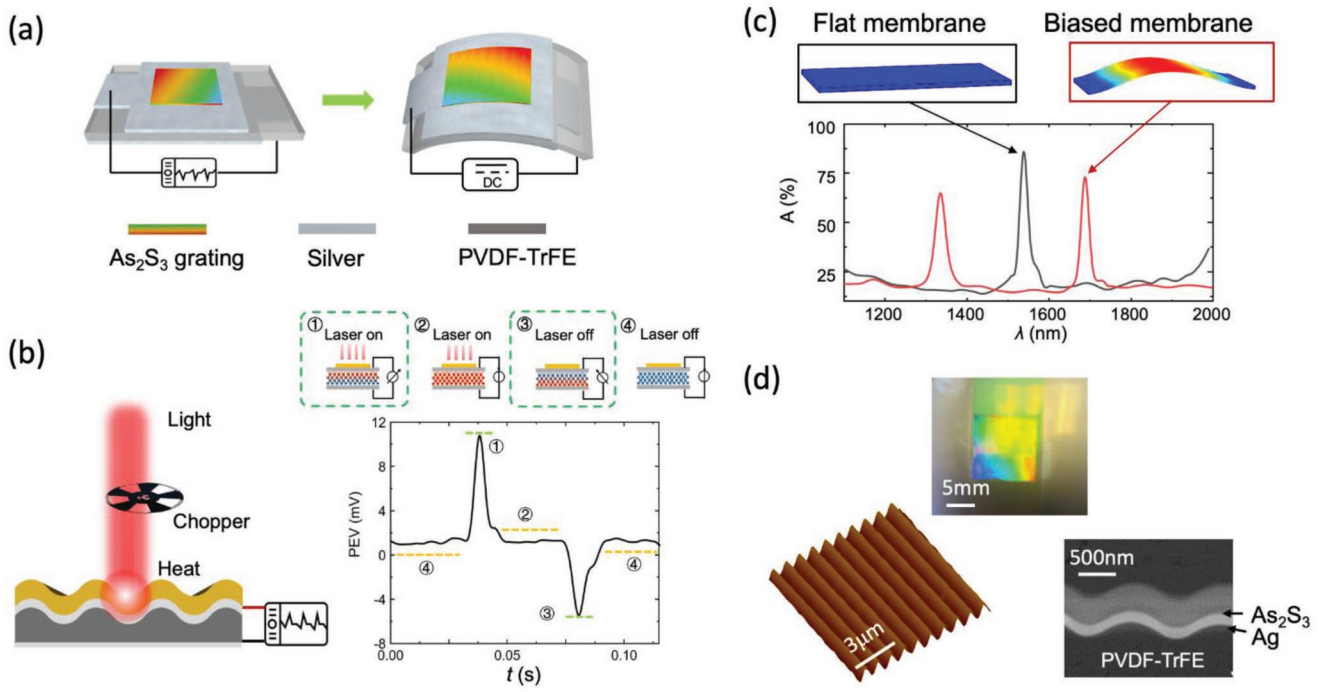


**Figure 1.** Design, operation, and fabrication of the tunable R-PED. a) Schematic illustration of the R-PED on a free-standing PVDF-TrFE membrane (left). A DC voltage can deform the membrane (right) and tune the R-PED's absorption. b) Resonant PEV signal generation. The modulated optical excitation causes the heating and cooling of the device and generates positive and negative PEV pulses. c) Tunable absorbance of the $As_2S_3$/Ag/PVDF-TrFE grating. The absorption spectra of a flat and bent R-PED are shown as the black and red curves, respectively. d) Photograph of the R-PED (left), AFM image (center), and cross-sectional SEM image (right) of the $As_2S_3$/Ag/PVDF-TrFE grating.

fluoride-trifluoroethylene (PVDF-TrFE) copolymer, which has a pyroelectric coefficient of approximately 0.025 C $m^{-2}$ $K^{-1}$.[25] Here, the R-PED was designed to absorb near-infrared (NIR) radiation around 1560 nm and generate PEV across the PVDF-TrFE membrane. The R-PED structure was numerically modeled and experimentally characterized for its absorption signatures, PEV spectra, responsivities, and input-output relationships. In addition, the R-PED structure can be tuned using a bias voltage applied to the PVDF-TrFE membrane. The bias voltage induced the membrane bending and thus changed the grating period and incident angle. The tuning capability of R-PED's absorbance and its PEV output at a specific wavelength was investigated.

## 2. Results and Discussion

### 2.1. Design and Fabrication of the R-PED

The design goal is to integrate the functions of narrowband light absorption, pyroelectric sensing, and piezoelectric tuning into one membrane. **Figure 1**a illustrates the R-PED structure, which is built upon a 15-μm-thick membrane. The PVDF-TrFE membrane was patterned with the sub-wavelength 1D grating structure. On top of the PVDF-TrFE grating, the thin film stack of Ag and $As_2S_3$ layers can effectively absorb NIR light at a specific wavelength. The NIR absorption can locally heat up the membrane, change the PVDF-TrFE's polarization, and generate a PEV across the Ag contacts on the top and bottom surface of the PVDF-TrFE membrane. The $As_2S_3$/Ag can be considered as an asymmetrical metal-cladding waveguide that supports the leaky mode resonance. As illustrated in Figure 1b, when the temperature is stabilized, the PEV signal drops back to zero. Without the light exposure, the device starts to cool down and outputs an opposite PEV signal. The response time and PEV amplitude largely depend on the thermal mass and heat capacity of the device. To reduce thermal mass, the R-PED was developed using the 15-μm-thick PVDF-TrFE membrane. At the resonant wavelength, the incidence of light can be coupled into the waveguide via the grating modulation, and the loss of Ag cladding causes a highly efficient light absorption shown in Figure 1c. During the optical heating phase, the PEV signal rises and reaches its maximum value at the equilibrium temperature.

The membrane R-PED was fabricated using a solvent-assisted imprint lithography process followed by the evaporation of Ag and $As_2S_3$ thin films. The details of the fabrication process are described in the Experimental Section, and the main steps are summarized in Figure S1, Supporting Information. Briefly, the PVDF-TrFE raw material was dissolved in dimethylformamide (DMF) and spun onto an Ag-coated glass substrate. The sample viscosity and spin speed were controlled to obtain the PVDF-TrFE thickness of 15 μm. The coated PVDF-TrFE film was then imprinted at 175 °C using the polydimethylsiloxane (PDMS) mold that carried the opposite grating pattern. After the imprint, the 100-nm Ag and 300-nm $As_2S_3$ films were


© 2021 The Authors. Advanced Optical Materials published by Wiley-VCH GmbH

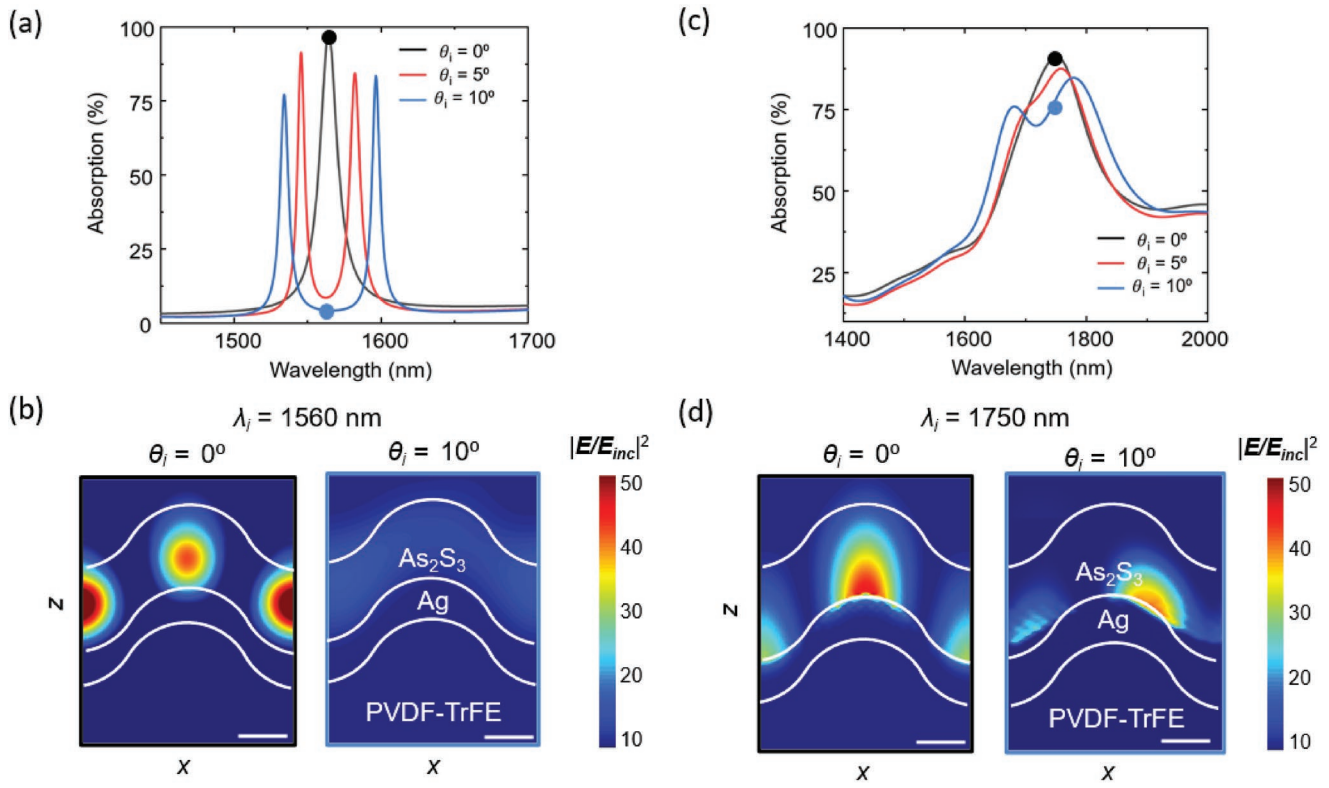


**Figure 2.** Numerical design of the resonant absorption grating. a) Simulated absorption spectra of the $As_2S_3$/Ag/PVDF-TrFE grating with a TE polarized incidence and $\theta_i = 0°$, 5°, and 10°, respectively. b) Calculated near field distributions for the TE modes with the absorption resonance when $\lambda_i = 1560$ nm and $\theta_i = 0°$ (left panel) and without the resonance when $\lambda_i = 1560$ nm and $\theta_i = 10°$ (right panel). The electric fields were plotted within one period of the grating. c) Absorption spectra of the TM mode resonances with $\theta_i = 0°$, 5°, and 10°, respectively. d) The local field distributions are associated with the TM modes and without the resonance effect in the left and right panels, respectively. Scale bar: 300 nm.

deposited using an e-beam evaporator. The stack consisting of Ag/PVDF-TrFE/Ag/$As_2S_3$ was carefully peeled off from the glass substrate to form the R-PED membrane. The photography, atomic force microscope (AFM), and scanning electron microscopy (SEM) images in Figure 1d shows the fabricated R-PED with a grating period of 1 µm and depth of 300 nm.

### 2.2. Numerical Design of the R-PED

To design an R-PED that can effectively absorb the telecom wavelength around 1.55 µm, the rigorous coupled-wave analysis (RCWA) was used to model the $As_2S_3$/Ag/PT grating. The details of the RCWA simulation model are given in the Experimental Section. **Figure 2** shows the calculated absorption spectra and near field distributions for the R-PED with the grating period, grating depth, Ag thickness, and $As_2S_3$ thickness of $\Lambda = 1$ µm, $d = 300$ nm, $t_{Ag} = 100$ nm, and $t_{As2S3} = 300$ nm, respectively. For the transverse electric (TE) mode, whose electric field is polarized along the $x$-axis, the absorption peak resides at the wavelength of $\lambda_{TE} = 1560$ nm and incidence angle of $\theta_i = 0°$ with a full-width half-maximum (FWHM) of 15 nm, as shown in Figure 2a. The resonant feature is sensitive to the incidence angle. The increase of $\theta_i$ resulted in the splitting and shifting of the resonant peaks towards red and blue spectral regions. The electric field distributions at given coupling conditions were calculated and plotted in Figure 2b. It can be seen that the near field of the TE mode ($|E_y|^2$) is confined in the $As_2S_3$ layer and significantly enhanced compared with the intensity of the incidence field. When the incidence light is coupled into a guided-mode resonance mode, the material loss of the Ag cladding causes the resonant absorption and effectively converts photon energy into heat.[22] In contrast, the right panel of Figure 2b shows the near field distribution at $\lambda = 1560$ nm and the incidence angle of $\theta_i = 10°$. Without resonant absorption, the local field intensity is weak, and light-to-heat conversion capability is limited. For the transverse magnetic (TM) modes, the absorption resonances locate around $\lambda_{TM} = 1750$ nm, as shown in Figure 2c. Figure 2d shows the near field distributions ($|E_x|^2 + |E_z|^2$) for two TM modes at $\lambda_{TM} = 1750$ nm and $\theta_i = 0°$ and 10°, respectively. Compared with the TE modes, the electric fields of the TM resonances mainly reside at the $As_2S_3$-Ag interface and exhibit a larger FWHM of 100 nm since the TM modes are associated with the surface plasmon resonance. Because the TE resonances exhibit an absorption resonance with narrower linewidth, the TE modes were chosen to develop the R-PED.

To estimate how the absorbed optical energy can raise the R-PED's temperature, we modeled the heat transfer process using a finite element method (FEM) simulation. The details of the thermodynamic FEM simulation are described in the Experimental Section. **Figure 3**a showed the temperature


© 2021 The Authors. Advanced Optical Materials published by Wiley-VCH GmbH

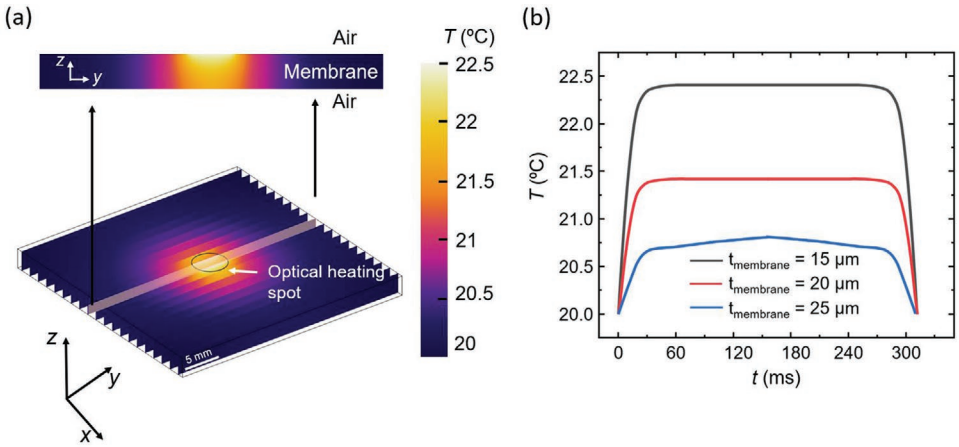


**Figure 3.** Thermodynamic simulation of light-induced temperature change. a) Temperature distributions along the vertical (top) and horizontal planes (bottom) of the PVDF-TrFE membrane. The 15-µm membrane was heated using a laser source at its center. b) Dynamic temperature changes as a function of time with membrane thicknesses of 15, 20, and 25 µm, respectively.

distribution around the R-PED membrane when the device was heated using a NIR laser beam ($\lambda = 1560$ nm and $P = 7.26$ mW) at its center. According to the result of prior electromagnetic simulation, we assumed the absorption coefficient of 80% and placed a 5.8 mW at the 1-mm-diameter heating spot. Under the ambient temperature of 20 °C, the NIR absorption can increase the membrane to 22.5 °C for the 15-µm-thick membrane. Figure 3b plots the dynamic temperature responses measured at the center of the membrane when the membrane was heated and subsequently cooled by shutting off the light source. The amount of temperature change and response time is mainly determined by the membrane thickness. As shown in Figure 3b, three membranes with a thickness of 15, 20, and 25 µm were simulated. For the 15-µm-thick membrane, the temperature can reach the equilibrium temperature of 22.5 °C within 32 ms.

### 2.3. Optical Characterization of the NIR R-PED

The resonant absorption features of the R-PED strongly depend on the coupling conditions, such as the wavelength and incident angle of the excitation light. Only when the coupling conditions are met, the device can absorb the excitation effectively. To characterize the absorption signatures, the optical dispersion diagram of the device was measured using the optical setup illustrated in **Figure 4**a. The sample was illuminated using a TE-polarized broadband light, and the reflectance ($R(\lambda)$) was analyzed using a fiber-coupled spectrometer. Because the Ag film's thickness exceeded its skin effect depth of 4.5 nm at $\lambda = 1560$ nm, there was no transmission through the device, and $T(\lambda) = 0$. The absorbance of the device was calculated using $A(\lambda) = 1 - R(\lambda)$. Figure 4b compares the measured and simulated absorption optical dispersion diagrams of the R-PED structure shown in Figure 1. The incident angle and wavelength ranged from 0° to 10° and 1450 to 1700 nm, respectively. For the TE-modes, two resonant bands can be seen across the NIR range. For the normal incidence at $\theta_i = 0°$, the device's absorption peak is located at $\lambda_r = 1560$ nm with the FWHM of 16 nm (Figure 4c). By tuning $\theta_i$ from 0° to 5°, the absorption resonance split into two resonances and moved to $\lambda_r = 1580$ and 1550 nm, respectively. The resonance modes can be shifted more by increasing the $\theta_i$ to 10°, as shown in Figure 4c. The upper and lower absorption bands showed the dispersion slopes of 4 and −2 nm/°, respectively.

### 2.4. Pyroelectric Detection Using the Tunable R-PED

#### *2.4.1. Resonant Pyroelectricity*

The PEV output of the device depends on the intensity, polarization, wavelength, and angle of incidence of the incoming light. We measured the PEV output signals using an oscilloscope when the R-PED device was illuminated by a tunable laser. The laser beam was collimated and polarized to excite the TE modes. **Figure 5**a plots the device output as a function of the time when the laser's intensity was modulated using a 50-ms-period square wave. The peak PEV was $V_{max} = 10$ mV with the laser's wavelength, power, and incidence angle of $\lambda = 1560$ nm, $P = 7.26$ mW, and $\theta_i = 0°$, respectively. At the red sections shown in Figure 5a, the laser light was on, and the device was heated. The device's PEV output reached its maximum value within 10 ms, representing a temperature rise of approximately 2.4 °C. After the temperature stabilized at equilibrium, the PEV signal dropped back to zero in 10 ms. When the laser was turned off, the device's temperature started to decrease to the ambient temperature during the cooling phase (the blue sections in Figure 5a). The temperature drop resulted in an opposite PEV with a $V_{min} = -7$ mV and peak to peak width of 0.1 s. The resonance-enhanced PEV phenomena on the PEV output were investigated for heating and cooling phases, respectively.

The spectral responsivities of the device were characterized at the incidence angle of $\theta_i = 0°$, 5°, and 10°, as shown in Figure 5b,c. At each angle of incidence, the laser wavelength was tuned from 1520 to 1620 nm with an increment of 5 nm. With the resonant absorption at $\theta_i = 0°$ and $\lambda_r = 1560$ nm, the device showed maximum responsibility of 1.42 mV $mW^{-1}$,


© 2021 The Authors. Advanced Optical Materials published by Wiley-VCH GmbH

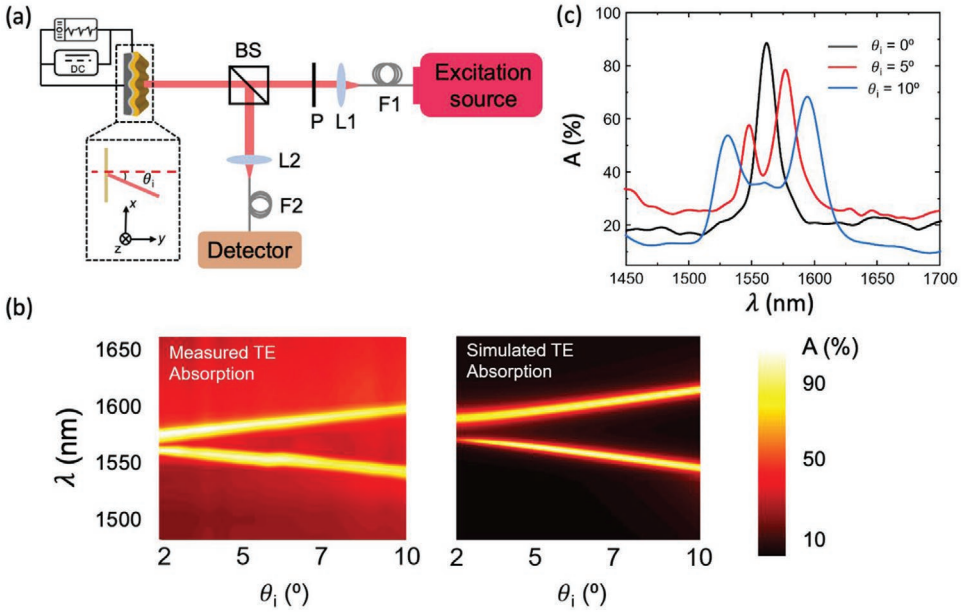


**Figure 4.** Characterization of R-PED's absorbance. a) Schematic diagram of the optical setup used to characterize the R-PED. The excitation source was coupled via optical fiber (F1), collimated using a lens (L1), polarized by a linear polarizer (P), and shined on the sample. The sample reflection passed through a beam splitter (BS) and was measured by the detector via a collimation lens (L2) and optical fiber (F2). b) Measured (left) and simulated (right) device absorption as a function of $\lambda$ and $\theta_i$ for the TE modes. c) Measured absorption spectra of the R-PED device when $\theta_i = 0°$, 5°, and 10°, respectively.

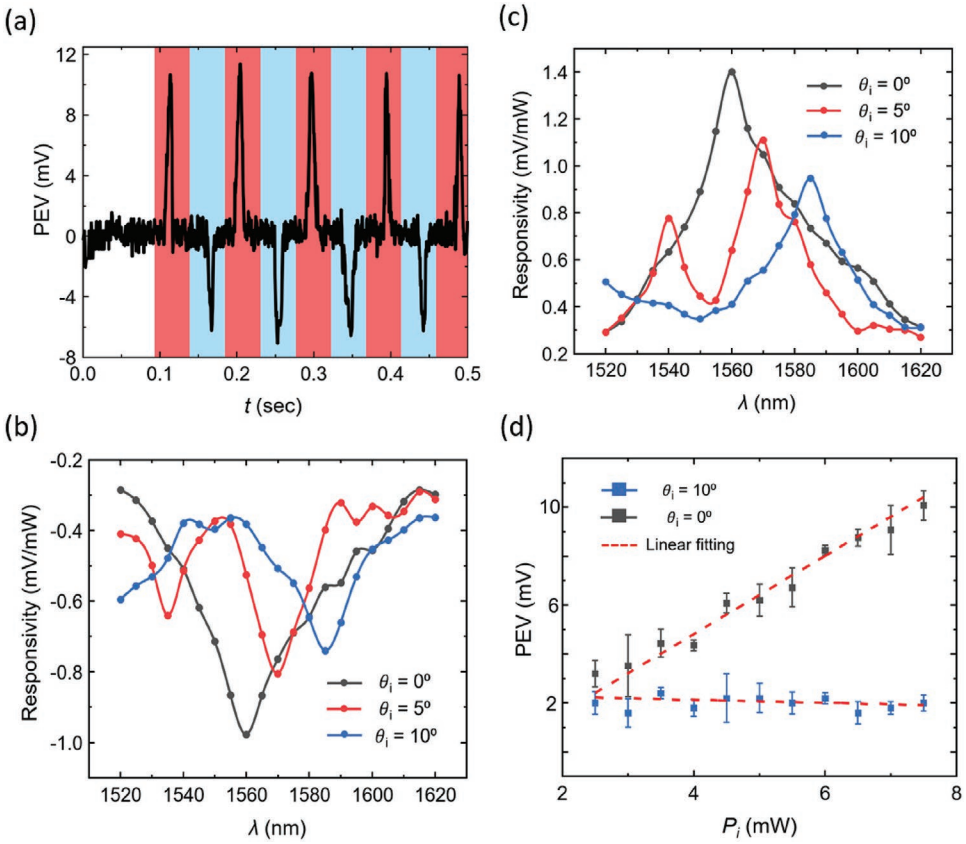


**Figure 5.** Characterization of photopyroelectric outputs. a) Measured PEV output as a function of time when the device was illuminated by a TE-polarized and intensity-modulated laser beam at $\lambda_i = 1560$ nm. b,c) Measured peak and dip PEV signals versus wavelength when the laser was turned on and off, respectively. The laser power was kept at $P = 7.26$ mW, and the emission wavelength was scanned from 1520 to 1620 nm. The R-PED's spectral response was measured at $\theta_i = 0°$, 5°, and 10°, respectively. d) Input and output relationship when the device was excited at the resonance condition of $\lambda_r = 1560$ nm and $\theta_i = 0°$ (black) and of the resonance condition of $\lambda_r = 1560$ nm and $\theta_i = 10°$.


© 2021 The Authors. Advanced Optical Materials published by Wiley-VCH GmbH

which was five times stronger than the off-resonance PEV of 0.25 mV mW$^{-1}$ at $\lambda = 1620$ nm (Figure 5b). The increase of incident angle to $\theta_i = 5°$ resulted in two peaks at $\lambda_{r1} = 1540$ nm and $\lambda_{r2} = 1570$ nm in the response curve. At $\theta_i = 10°$, one of the PEV peaks shifted to 1590 nm, and the other one moved out of the laser's tuning range. The PEV spectra agree well with the R-PED's absorbance spectra shown in Figure 4c. During cooling phases, the polarity of the PEV signal was inverted, and the negative resonant PEV peaks can be seen in Figure 5c. Figure 5d compares the PEV input-output relationships for the on-resonance ($\theta_i = 0°$ and $\lambda_i = 1560$ nm) and off-resonance ($\theta_i = 10°$ and $\lambda_i = 1560$ nm) cases, respectively. The laser emission power scanned from 2.5 to 7.25 mW, and the peak PEV signals were plotted. For both cases, the PEV output varied linearly versus the excitation laser power. The on-resonance input-output relationship showed a slope of 1.36 mV mW$^{-1}$, which is 45 times higher than the off-resonance slope of 0.03 mV mW$^{-1}$. Since the Johnson–Nyquist noise was the dominant noise source, the noise spectral density (NSD) is $NSD = \sqrt{4Rk_BT}$, where $T$ is the room temperature of 20 °C, $R = 470\ \Omega$ is the device resistance, and $k_B$ is the Boltzmann's constant. The NSD of the R-PED sensor was 6 μV Hz$^{-1/2}$ at room temperature. The noise equivalent power (NEP) can be calculated using the NSD divided by the voltage responsivity. The NEP spectra of the device at different angles of incidence are plotted in Figure S4, Supporting Information. The minimal NEP value of 13 μW Hz$^{-1/2}$ was found at the resonance of $\lambda_r = 1560$ nm and $\theta_i = 0$ °.

### 2.4.2. Tuning of Resonant Absorption

As a piezoelectric material, the PVDF-TrFE membrane produces mechanical stress when a bias voltage is applied across it. The strain mismatch between the membrane and $Ag/As_2S_3$ thin films can bend the membrane, as illustrated in **Figure 6**a. The controlled membrane deformation can be employed to tune the resonance absorption characteristics by increasing the grating period and the angle of incidence, which is similar to the piezoelectric photonic crystal resonators.[26] Figure 6b compares the FEM simulation results of membrane displacements when the bias voltage of 0, 5, 10, and 15 V were applied. The membrane was suspended by fixing two edges along the *y*-axis, and the membrane edges along the *x*-axis were free to move. The amount of membrane displacement along the *z*-axis was present by the color scale. Figure 6c plots the change of grating period as a function of bias voltage. The effect of membrane bending on the coupling angle was characterized

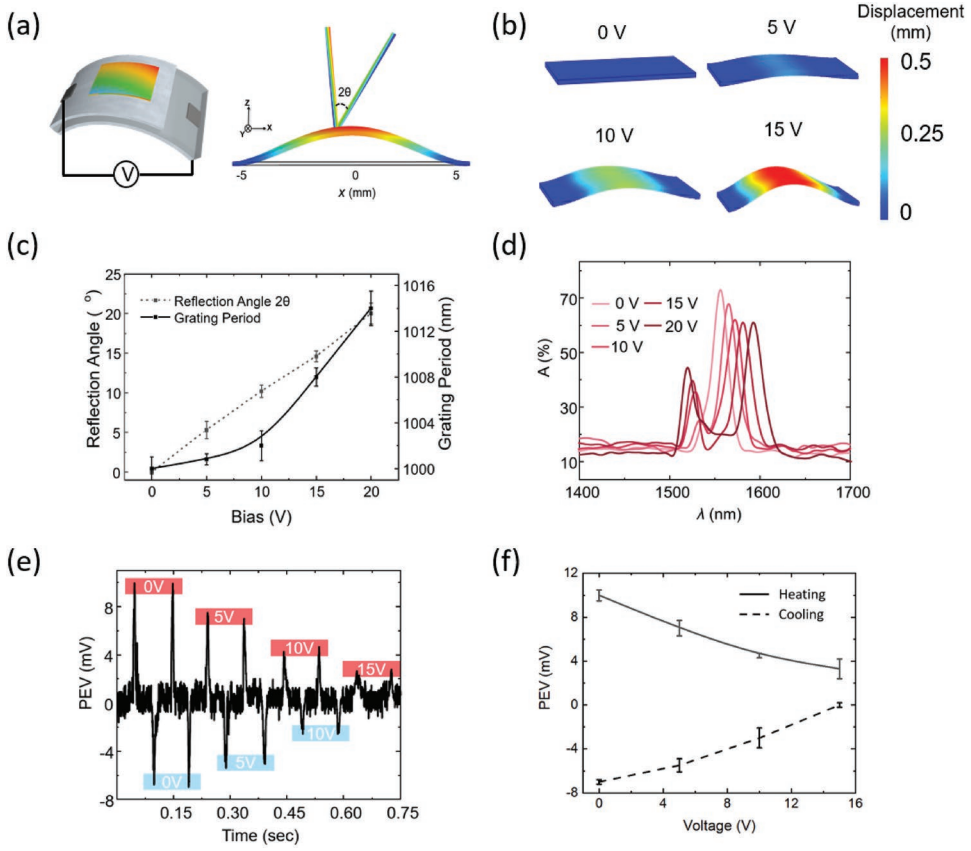


**Figure 6.** Tuning of absorption resonance by biasing the PVDF-TrFE membrane. a) Schematic and simulated membrane bending caused by a bias voltage. b) Simulated membrane deforming when different bias voltages were applied to the PVDF-TrFE membrane. c) Measured changing of membrane curvature and calculated change of grating period as a function of bias voltage. d) R-PED absorption spectra when the bias voltage of 0, 5, 10, 15, and 20 V were applied to the membrane. e) PEV output waveforms when the four different bias voltages were applied across the membrane. f) Measured PEV outputs versus bias voltage for heating and cooling processes, respectively.


© 2021 The Authors. Advanced Optical Materials published by Wiley-VCH GmbH

by measuring the laser beam deflection. The details of the deflection angle measurement are given in the supplementary materials (Figure S2, Supporting Information). The reflection angle $\theta = \sin^{-1}(0.5L'/d)$, where $d$ represents the membrane displacement along the $z$-axis, was calculated by simulation. Then the $L'$, which is the length of the membrane after bending, can be calculated, as shown in Figure 6c. Figure 6d compares the measured absorption spectra of TE modes with the bias voltage ranging from 0 to 20 V. Based on results, we calculated the change of the grating period, which is proportional to the membrane length along the $y$-axis: $\Delta\Lambda = (L'-L)/L$, where $L$ is the length of the membrane, the period changing of the grating is about 0.8 nm $V^{-1}$. Without a zero bias, the absorption resonance is located at $\lambda_r$ = 1560 nm with an FWHM of 16 nm. Owing to the voltage-induced grating period and radius changes, the resonance mode split and shifted in the way given by the dispersion relationship (Figure 4c). With the bias voltage of 20 V, the absorption peak moved to 1597 and 1540 nm. For the resonance modes that shifted towards the red and blue directions, the voltage tuning sensitivities are 1.85 and −2 nm $V^{-1}$, respectively.

#### 2.4.3. Tuning of R-PED's PEV Output

The capability of controlling the device's absorption enabled the development of a tunable R-PED. Figure 6e shows the absorption spectra of the tunable PVDF sensor when the bias voltage (from 0 to 15 V) was applied to the device, and Figure 6f presents the PEV outputs versus bias voltage for heating and cooling processes. To demonstrate the tunable pyroelectric effect, we applied the DC bias voltage to bend the membrane and, in the meantime, measured its PEV output using the oscilloscope. The device was illuminated using the NIR laser ($\lambda$ = 1560 nm, $\theta_i = 0°$, and $P$ = 7.26 mW), whose intensity was modulated at 10 Hz. Figure 6e plots the R-PED's dynamic output. Without the bias voltage, the device can absorb the laser light efficiently and generate strong PEV output of 10.2 mV. When the bias increased from 0 to 15 V, the device absorption was reduced, and the PEV output consequently decreased from 10.2 to 2.9 mV. At 20 V, the device absorption was only 18% at 1560 nm due to the resonance shifting, and the PEV signal was too weak to be distinguished from its noise floor.

## 3. Conclusion

The narrowband pyroelectric sensor demonstrated in this work seamlessly integrated the resonant grating absorber and the pyroelectric material to detect the change of NIR excitation. The Ag-clad $As_2S_3$ grating was able to absorb radiation around 1560 nm with a bandwidth of 15 nm and effectively convert the absorbed optical energy into heat. The light-induced temperature variations generated PEV signals from the PVDF-TrFE membrane. The results showed that the PEV signal is sensitive to the coupling of infrared radiation and the absorption resonance modes. With the resonant absorption at 1560 nm, the device showed the responsivity of 1.4 mVmW$^{-1}$, which was fifty times higher than the device responsivity without incurring any resonance mode. Furthermore, we studied the tuning capability of the resonant absorber by applying a bias voltage across the PVDF-TrFE membrane. Because the bias voltage can induce internal mechanical stress and deform the membrane, the resonant absorption can be tuned within the range of 50 nm and sensitivity of 1.85 nm $V^{-1}$. The tunable resonant absorption was utilized for the development of the tunable R-PEDs.

In future work, the device performances, such as the response time, bandwidth, and sensitivity, will be improved from the following three aspects. First, materials with a higher pyroelectric coefficient will be adopted in the R-PEDs to replace the PVDF-TrFE substrate. The resonant grating structure can be fabricated on thin films with a high pyroelectric coefficient, such as barium titanate, aluminum nitride, cesium nitrate, and lithium tantalite, to enhance PEV output. Second, by optimizing the grating structures, the bandwidth and response time of the R-PED can be further reduced. Last, an array of R-PEDs with different spectral bands can be integrated on one chip to detect multiple wavelengths simultaneously for multiband sensing applications.

## 4. Experimental Section

*Fabrication Process*: The hot embossing approach, shown in Figure S1, Supporting Information, was used to fabricate the subwavelength grating structure in the PVDF-TrFE membrane.[27] The 1-µm-period grating was replicated from a holographic grating film (#40-267, Edmund Optics) to the PDMS mold. Before the embossing process, the PVDF-TrFE film was spun onto a silver-coated glass substrate. The 100-nm silver layer was evaporated using an electron beam evaporator (BJD-1800, Temescal) to facilitate the release of the PVDF-TrFE membrane. The PVDF-TrFE powder was dissolved in DMF at 75 °C to 15%(w/v%). The dissolved PVDF-TrFE was spin-coated on the silver-coated glass slide at a spinning speed of 4000 rpm for 45 s. After the spin coating, the sample was baked at 160 °C for 4 h to completely evaporate DMF. Then, the film was embossed using the PDMS mold at the glass transition temperature of PVDF (≈ 175 °C) on a hotplate under a pressure of 80 kPa for 20 s. After being cooled down to room temperature, the PDMS mold was peeled away to leave the grating pattern on top of the PVDF-TrFE film. Following the molding process, the Ag and $As_2S_3$ thin films were deposited using the evaporator. The thickness and refractive index of the Ag and $As_2S_3$ layers were measured using a spectroscopic ellipsometer (J.A. Woollam Co., Inc.). To release the membrane, the stack of Ag/PVDF-TrFE/$As_2S_3$/Ag films were carefully peeled off from the glass substrate and suspended on a 5 mm × 5 mm frame for tests.

*Numerical Modeling*: The RCWA simulation model consisted of a single period of the 1D grating pattern along the $x$-axis. The refractive index ($n(\lambda)$) and extinction coefficient ($k(\lambda)$) of Ag and $As_2S_3$ thin films were interpolated using the results obtained from the ellipsometry measurement as shown in Figure S3, Supporting Information. The incidence light was linearly polarized along the $x$-axis and $y$-axis for the TM and TE modes, respectively. The model output reflectance ($R(\lambda)$) and transmittance ($T(\lambda)$) were in the wavelength range of 1400 to 1700 nm. The absorption spectra were calculated using $A(\lambda) = 1-R(\lambda)-T(\lambda)$. At the resonance wavelength, the near field distribution was plotted using the total electric field of $E(x,z) = \sqrt{|E_x|^2 + |E_y|^2 + |E_z|^2}$.

The temperature distribution profile across the PVDF device was modeled using finite element analysis (COMSOL Multiphysics 5.3). The simulation domain contained the membrane stack of PVDF, silver, and $As_2S_3$ layers with the thickness of 15 µm, 100 nm, and 300 nm, respectively. The simulation domain was discretized using 4-noded tetrahedral meshes and was truncated using the open boundary on all sides of the membrane. The open boundary meant the membrane was


© 2021 The Authors. Advanced Optical Materials published by Wiley-VCH GmbH

in contact with the surrounding air at room temperature ($T = 20$ °C). A constant heat source was applied on the top surface of the membrane with a spot diameter of 1 mm. Assuming the excitation power of 7.26 mW and the absorption coefficient of 80%, the input power of the heat source was 5.8 mW. A time-dependent solver was used to solve Poisson's equation for heat transfer, $\frac{\partial^2 T}{\partial x^2}+\frac{\partial^2 T}{\partial y^2}+\frac{\partial^2 T}{\partial z^2}-\frac{\rho c_p}{k}\frac{\partial T}{\partial t}+\frac{\dot{e}_{gen}}{k}=0$, where $T$ represents the temperature value at each mesh node, $\dot{e}_{gen}$ is the rate of heat generation ($Wm^{-3}$) at the heat source, $k$ denotes the heat conductivity, $\rho$ is the material density, and $C_p$ is the specific heat capacity. Interfaces between the materials were treated using the equivalent conductivity, $K_s=\frac{2k_1k_2}{k_1+k_2}$, where $k_1$ and $k_2$ denote the heat conductivities of the materials in contact, respectively. The heat conductivity, heat capacity at constant pressure, and density of the materials, including air, Ag, $As_2S_3$, and PVDF, were taken from the COMSOL's built-in material library.

The membrane deformation under a DC bias was also simulated using COMSOL. The membrane was suspended by fixing two edges that were perpendicular to the $x$-axis, and the other two edges can move freely, as shown in Figure 6a. The bias voltage was applied across the silver electrodes to displace the membrane. The solver calculated the membrane displacement using the piezoelectric equation and the strain-displacement relationship: $s^E\mathrm{T}+d^T\mathrm{E}=\frac{1}{2}[(\nabla u)^T+\nabla u]$, where $s^E$ represents the elastic compliance, T is the stress, $d^T$ denotes the piezoelectric charge constants, E is the static electric field, and $u$ represents the membrane displacement vector. The Young's modulus, Poisson's ratio, and density of the materials, including Ag, $As_2S_3$, and PVDF, were given by the COMSOL's built-in material library.

*Absorption and Band Diagram Measurements*: The absorption characteristics of the device were measured using a home-built setup. Because the Ag cladding layer was sufficiently thick, the transmission through the device was nearly zero. The absorption spectra were obtained by calculating $A(\lambda)=1-R(\lambda)$. To measure $R(\lambda)$, the device was illuminated using a fiber-coupled broadband light source (LS-1, Ocean Optics, Inc.), and its reflection was analyzed using a NIR spectrometer (NIRQuest, Ocean Optics). To adjust the angle of incidence, the sample was mounted on a rotation stage. The sample reflectance was calculated with regard to the reflection of an Ag mirror, which served as the reference. To plot the band diagram, the reflection spectra were collected by rotating the sample over the angle range of $0° < \theta_i < 10°$ with an increment of 0.5°.

*PEV Measurement Setup*: The wavelength-dependent measurement was performed using a tunable laser source (ANDO, AQ4321). The lasing wavelength can be scanned from the NIR range of 1520 to 1560 nm, and its emission power can be adjusted from 0 to 7.26 mW. The tunable laser output was collimated and polarized using the linear polarizer in front of the device. The device was attached to a kinetic mount, which was placed on a rotation stage to precisely adjust the angle of incidence. The PEV outputs from the membrane were measured using the oscilloscope (2000X, Keysight Technologies) when the outputs of the tunable laser were modulated at 10 Hz. To tune the PVDF-TrFE device, the device was biased using a DC power supply (E3631A, Agilent).

## Supporting Information

Supporting Information is available from the Wiley Online Library or from the author.

## Acknowledgements

This work was supported by the National Science Foundation under Award Nos. ECCS 17-11839 and ECCS 16-53673. Any opinions, findings, and conclusions, or recommendations expressed in this material are those of the author(s) and do not necessarily reflect the views of the National Science Foundation.

## Conflict of Interest

The authors declare no conflict of interest.

## Data Availability Statement

Research data are not shared.

## Keywords

guided-mode resonance, photonic crystals, photothermoelectric effect, resonant absorbers

Received: June 8, 2021
Revised: July 30, 2021
Published online: September 2, 2021

[1] A. Mandelis, M. M. Zver, *J. Appl. Phys.* **1985**, *57*, 4421.
[2] S. Pandya, G. Velarde, L. Zhang, J. D. Wilbur, A. Smith, B. Hanrahan, C. Dames, L. W. Martin, *NPG Asia Mater* **2019**, *11*, 26.
[3] Y. Yang, H. Zhang, G. Zhu, S. Lee, Z.-H. Lin, Z. L. Wang, *ACS Nano* **2013**, *7*, 785.
[4] T. D. Dao, S. Ishii, A. T. Doan, Y. Wada, A. Ohi, T. Nabatame, T. Nagao, *Adv. Sci.* **2019**, *6*, 416.
[5] M. Kumar, D.-K. Ban, J. Kim, *Mater. Lett.* **2018**, *225*, 46.
[6] Y. Wang, J. Song, L. Dong, M. Lu, *J. Opt. Soc. Am. B* **2016**, *33*, 2472.
[7] J. Yun, M.-H. Song, *IEEE Sens. J.* **2014**, *14*, 1482.
[8] A. G. Paulish, A. V. Gusachenko, A. O. Morozov, V. A. Golyashov, K. V. Dorozhkin, V. I. Suslyaev, *Sens. Rev.* **2020**, *40*, 291.
[9] Q. Li, S.-H. Ding, R. Yao, Q. Wang, *J. Opt. Soc. Am. A* **2010**, *27*, 2381.
[10] C. Ranacher, C. Consani, A. Tortschanoff, L. Rauter, D. Holzmann, C. Fleury, G. Stocker, A. Fant, H. Schaunig, P. Irsigler, T. Grille, B. Jakoby, *Sensors* **2019**, *19*, 2513.
[11] Z. Wang, R. Yu, C. Pan, Z. Li, J. Yang, F. Yi, Z. L. Wang, *Nat. Commun.* **2015**, *6*, 8401.
[12] J. Y. Suen, K. Fan, J. Montoya, C. Bingham, V. Stenger, S. Sriram, W. J. Padilla, *Optica* **2017**, *4*, 276.
[13] H. Lu, B. Sadani, G. Ulliac, C. Guyot, N. Courjal, M. Collet, F. I. Baida, M.-P. Bernal, *Opt. Express* **2013**, *21*, 16311.
[14] N. Neumann, M. Ebermann, S. Kurth, K. Hiller, *J. Micro/Nanolithogr. MEMS MOEMS* **2008**, *7*, 021004.
[15] M. Leidinger, C. S. Werner, W. Yoshiki, K. Buse, I. Breunig, *Opt. Lett.* **2016**, *41*, 5474.
[16] S. J. Kim, M. L. Brongersma, *Opt. Lett.* **2017**, *42*, 5.
[17] S. S. Wang, R. Magnusson, *Appl. Opt.* **1993**, *32*, 2606.
[18] X. Yin, J. Jin, M. Soljačić, C. Peng, B. Zhen, *Nature* **2020**, *580*, 467.
[19] V. Karagodsky, F. G. Sedgwick, C. J. Chang-Hasnain, *Opt. Express* **2010**, *18*, 16973.
[20] Z. S. Liu, S. Tibuleac, D. Shin, P. P. Young, R. Magnusson, *Opt. Lett.* **1998**, *23*, 1556.
[21] L. Liu, R. Mahmood, L. Wei, A. C. Hillier, M. Lu, *Nanotechnology* **2019**, *30*, 045203.
[22] H. Monshat, L. Liu, M. Lu, *Adv. Opt. Mater.* **2018**, *7*, 1801248.
[23] L. Wei, J. Qian, L. Dong, M. Lu, *Small* **2020**, *16*, 2000472.
[24] L. Li, H. Lin, S. Qiao, Y. Zou, S. Danto, K. Richardson, J. D. Musgraves, N. Lu, J. Hu, *Nat. Photonics* **2014**, *8*, 643.
[25] P. Ueberschlag, *Sens. Rev.* **2001**, *21*, 118.
[26] G. G. See, A. Gal, L. Xu, R. Nuzzo, S. Gong, B. T. Cunningham, *Opt. Express* **2017**, *25*, 25832.
[27] W. K. Schomburg, K. Burlage, C. Gerhardy, *Micromachines* **2011**, *2*, 157.


© 2021 The Authors. Advanced Optical Materials published by Wiley-VCH GmbH